

Article

Elevation Angle Characterization for LEO Satellites: First and Second Order Statistics

Juan Misael Gongora-Torres ^{*,†} , Cesar Vargas-Rosales [†] , Alejandro Aragón-Zavala [†] 
and Rafaela Villalpando-Hernandez [†] 

Tecnologico de Monterrey, School of Engineering and Science, Monterrey 64849, Mexico

* Correspondence: misael.gongora@tec.mx

† These authors contributed equally to this work.

Abstract: The elevation angle θ is relevant for the Low Earth orbit (LEO) satellite communications since it is always changing its relative position with respect to fixed Earth stations (ES's), and this affects the link length and received power, P_R . This article provides a new methodology to compute the probability density function (PDF) and cumulative distribution function (CDF) of the elevation angle, θ , for diverse ES locations. This methodology requires as input parameters an ES latitude, ϕ , an orbit inclination value, i , and an orbit altitude, h . The elevation angle is characterized through a well known random variable, which facilitates the computation of the first and second-order statistics, and helps to determine the expected value and measures of dispersion of the angle θ for a particular ES location. The proposed methodology allows an easy and quick calculation of the elevation angle's CDF, facilitating comparisons against CDF's of more ES's located at different latitudes, and longitudes, λ ; as well as the comparisons of CDF's of the elevation angle produced by different orbits. Extensive simulation results are summarized in a small table, which allows computation of the elevation angle's CDF and PDF for multiple ES locations without requiring of simulations and statistical fitting. Finally, the proposed methodology is validated through an extensive error analysis that show the suitability of the obtained results to characterize the elevation angle.

Keywords: Low Earth orbit (LEO); elevation angle; satellite communications



Citation: Gongora-Torres, J.M.; Vargas-Rosales, C.; Aragón-Zavala, A.; Villalpando-Hernandez, R. Elevation Angle Characterization for LEO Satellites: First and Second Order Statistics. *Appl. Sci.* **2023**, *13*, 4405. <https://doi.org/10.3390/app13074405>

Academic Editors: Simone Battistini, Filippo Graziani and Mauro Pontani

Received: 26 February 2023

Revised: 18 March 2023

Accepted: 21 March 2023

Published: 30 March 2023



Copyright: © 2023 by the authors. Licensee MDPI, Basel, Switzerland. This article is an open access article distributed under the terms and conditions of the Creative Commons Attribution (CC BY) license (<https://creativecommons.org/licenses/by/4.0/>).

1. Introduction

The characterization of the elevation angle, θ is relevant for low Earth orbit (LEO) satellite communications since this parameter is directly related to the varying distance between the satellite and Earth station (ES), and affects the link total attenuation. The elevation angle description through an analytical expression is a difficult problem addressed in [1,2] which has received less attention in the literature.

Nonetheless, this parameter is directly related to the link performance and channel characterization of LEO satellites. The LEO channel characterization has also received less attention than the geostationary (GEO) satellite channel and just few models such as [3] have been specifically developed and published to consider the elevation angle variations introduced at LEO. The lack of LEO channel models accounting for the always-changing elevation angle have resulted in just a few channel models available in the literature for LEO satellites and specially for small satellites as mentioned in [4].

LEO satellites are increasing their numbers and role as an enabling technology for Internet of Things (IoT), 5G, 6G, and next generation wireless networks aimed to provide global coverage with very low latency [5]. Then it is relevant to develop methodologies to analyze and compare the link performance and channel characteristics considering the variations introduced by the always-changing elevation angle.

The always-changing elevation angle condition has been a limitation to analyze the link budget and channel of LEO satellites, and common approaches to characterize it

have followed segmentation in best and worst-case of the elevation angle [6], instead of analyzing the short and long term behavior of the elevation angle as an analytical function. However, some emerging problems, such as efficient power management [7], related to LEO satellites have made evident the necessity of having a way to characterize the elevation angle as an analytical function.

The observed elevation angle, θ , is always-varying for LEO satellites and can be described as a function of time, $\theta(t)$, for intervals in which a satellite is visible. The calculation of θ for a given position can be deterministically obtained with mathematical procedures developed in orbital mechanics books [8] and widely implemented in software for space dynamics simulations. However, it is important to note that even with accurate predictions of θ (accounting for contacts in several days or months), the relations between one contact and another, as well as the long term behavior of the elevation angle can be hardly described without randomness. Thus, appropriate use of probability theory becomes a great tool to analyze the behavior of the elevation angle, θ , in the long term.

The elevation angle, θ , is usually defined for an ES as the angle (above the local horizon) at which the satellite is visible, and within the interval of 0° to 90° , $\theta \in (0^\circ, 90^\circ]$, regardless of its azimuth. The minimum value of θ at which communication is possible is often called θ_{min} (subject to $\theta_{min} \geq 0^\circ$), similarly, the maximum value of θ that can be observed from the ES is called θ_{max} (subject to $\theta_{min} \leq \theta_{max} \leq 90^\circ$). We can define a random variable, r.v., to take possible values of θ , such that $\theta \in (\theta_{min}, \theta_{max}]$ as Θ .

The probability density function, PDF, and cumulative distribution function, CDF, of the elevation angle, $f_\Theta(\theta)$ and $F_\Theta(\theta)$, respectively, are useful functions to characterize the LEO channel since the elevation angle affects the received power level, P_R . The reasoning behind that is that θ depends on the distance from the satellite to the ES, $r_{S,E}$. Then, at greater link distances, it can be expected to have a lower received power, P_R , (of the transmitted signal from the satellite) than at shorter distances.

The distance between a LEO satellite and an ES, $r_{S,E}$, can vary several thousands of kilometers from a low value of θ to a high value of θ . Figure 1a shows the extreme cases for the elevation angle in a LEO satellite link. Those extreme cases are not necessarily met at every contact, but represent the best and worst length-scenarios in a long period. Path lengths between the ES and satellite, $r_{S,E}$, are described in this figure using the variable r_i , $i \in \{1, 2, 3\}$. The figure also shows that at low values of θ the path length is larger and the received power, P_R is at its minimum value. This last implication between the elevation angle, θ , the received power, P_R , and the link length, $r_{S,E}$, assumes some constraints explained in detail in [9].

Figure 1b shows the typical-case for the elevation angle, where the value of θ is not necessarily at its minimum nor at its maximum, but it can be at any value within the range $\theta \in [\theta_{min}, \theta_{max}]$. Since the elevation angle of a LEO satellite appears as always-varying from an ES's, it is convenient to determine statistical indicators of its behavior, such as its expected value, $E[\cdot]$, median, $MED[\cdot]$, standard deviation, $SD[\cdot]$; and how often does the elevation angle will be above or below a threshold, or within a region of interest, for example, using its quantiles nQ . In addition, since the elevation angle variations are directly related to the link length, the elevation angle for LEO satellites is also directly related to the variations of the received power P_R at an ES, as described in [9].

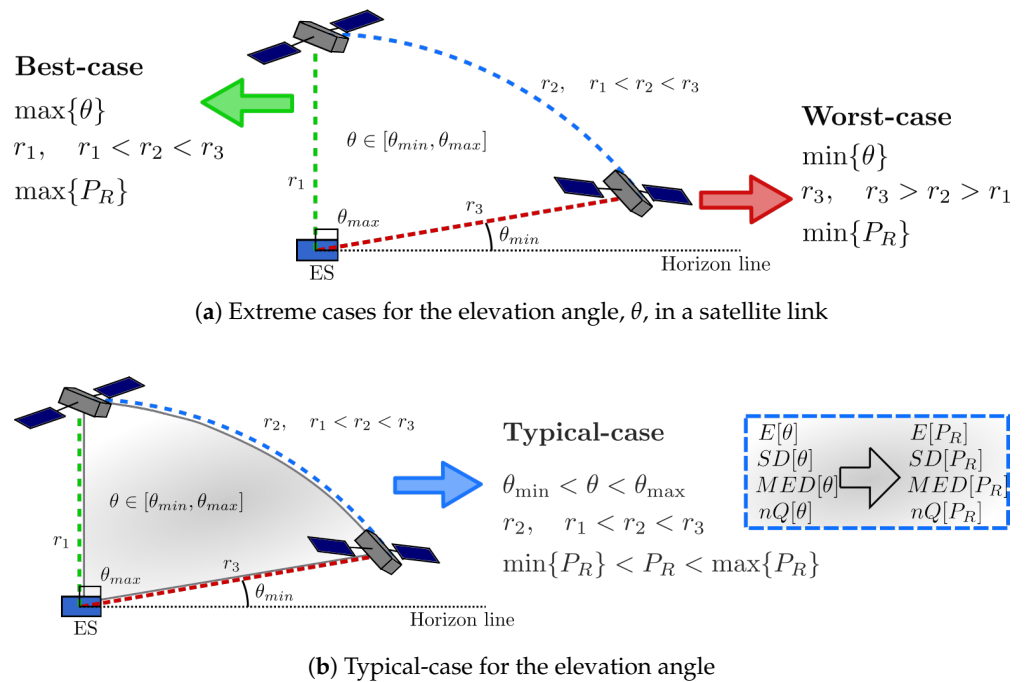


Figure 1. Elevation angle cases for LEO satellite systems: (a) The values of θ_{min} and θ_{max} are usually related to the best and worst case of the received power, P_R , at an ES; nonetheless, those cases are rare and represent the extremes of θ . (b) The elevation angle of a LEO satellite system as observed from an ES is always-varying; then, it is more convenient to analyze its behavior through statistical tools.

1.1. Contributions

The elevation angle characterization is relevant for LEO satellites because it is an always-changing variable for those communication systems. The effects of the elevation angle variations are observable in the received power, link quality, and channel behavior; then, an accurate characterization of this variable is a topic of interest for planning and implementation of LEO satellite systems.

In this article, we have addressed the characterization of the elevation angle for LEO satellites, by obtaining its PDF and CDF, as well as the derivation of its first and second order statistics. First and second order statistics are relevant to evaluate the suitability of different LEO orbits and to determine which orbits are more convenient to provide coverage for a particular application or Earth station location.

In addition, we have developed an extensive analysis to validate our results, and we include supplementary materials containing elevation angle times series. The supplementary materials will facilitate reproducibility of our work, and will allow future research based on our proposed methodology and results.

1.1.1. Contribution 1

This document shows the feasibility of using a random variable to characterize the elevation angle behavior for LEO satellites with different orbit configurations. The suitability of using the proposed random variable is verified through an extensive error analysis with diverse orbit configurations.

1.1.2. Contribution 2

The PDF and CDF of the elevation angle can be obtained as proposed in [1,2]. Nonetheless, this document describes a methodology to obtain the PDF and CDF parameters of the elevation angle distribution for different orbit configurations and ES locations using a well-known random variable. The proposed random variable facilitates analytical manipulation as well as computation of the probabilities of occurrence of the elevation angle at

specific values. A small table containing the resultant parameters to characterize multiple LEO orbits configurations as observed from multiple ES's is included.

1.1.3. Contribution 3

The expected value of the elevation angle and its measures of dispersion are relevant for planning and implementation of LEO satellite systems, since the received power varies according to the elevation angle. This document describes an analytical methodology to obtain the first and second order statistics of the elevation angle for different orbit configurations and ES locations, which, to the best of our knowledge are not available in the literature and were just utilized for a specific case in [9].

1.2. Outline

The remaining of the article is organized as follows: Section 2 introduces the theoretical fundamentals required to understand the subsequent sections; Section 3 describes the developed methodology to characterize the elevation angle behavior through $f_{\Theta}(\theta)$ and $F_{\Theta}(\theta)$; Section 4 contains the main results; and Section 5 concludes analyzing the obtained results and opportunities for future work. Figure 2 shows the main structure of the document.

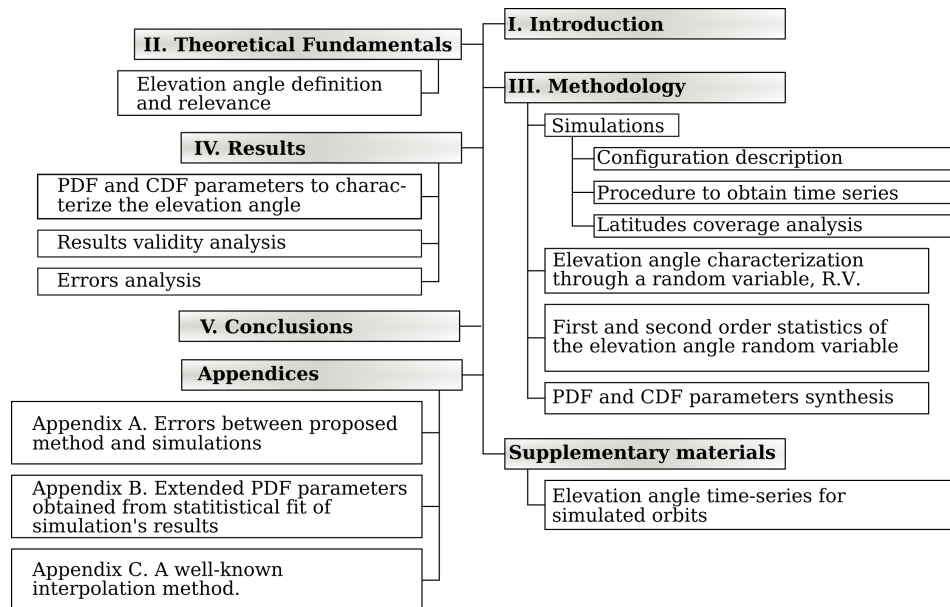


Figure 2. Basic structure and contents of this article.

2. Materials and Methods

2.1. Elevation Angle Definition

The elevation angle, θ , for an ES can be defined as the angle between the local horizon and the satellite. Several sources such as [10–12] contain expressions to calculate θ from geometrical relations between the satellite and the ES instantaneous positions. One of those definitions is as follows

$$\theta = \arctan \left(\frac{\cos \Delta \cos \phi_{ES} - (r_{E,O}/r_{S,O})}{\sqrt{1 - \cos^2 \Delta \cos^2 \phi_{ES}}} \right), \tag{1}$$

where $r_{E,O}$ and $r_{S,O}$ are the distances from the center of the Earth, O , to the ES and the satellite, respectively; ϕ_{ES} is the latitude at which the ES is located (in degrees); M is the subsatellite point, which corresponds to the latitude and longitude of the satellite instantaneous position; and Δ is the difference in longitude between the ES and M (in degrees). Figure 3a shows a derivation of θ based on (1).

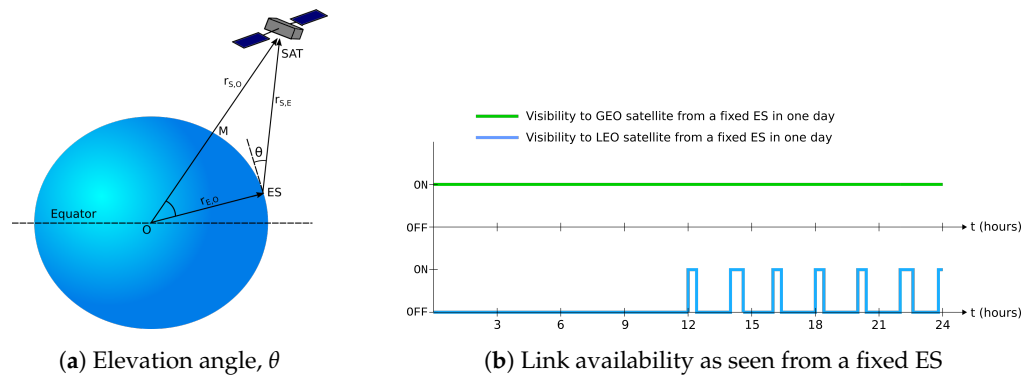


Figure 3. LEO characteristics: (a) Graphical representation of the always-varying elevation angle, θ , and (b) an On-Off model showing the link availability for a LEO satellite vs a GEO satellite during a random day.

2.2. Relevance of the Elevation Angle for the Satellite Channel

LEO satellites differ to those at GEO in its relative position as seen from a fixed ES. Whereas GEO satellites appear as fixed, those at LEO appear as always-moving points in the sky or are absent causing link unavailability. Link availability can be seen as an ON-OFF process, where the link is ON if the satellite is visible in the sky, and it is OFF if the satellite is absent. Figure 3b shows the ON-OFF process for both a LEO and GEO satellite.

In addition to the short visibility that LEO satellites have, conditions in this lapse are always varying as a consequence of the changing position of the satellite. When the satellite is first visible from an ES, it is at the largest distance supported by the link, then, the satellite starts approaching the ES until reaching the shortest distance in that particular contact. Finally, the satellite moves away after being at its minimum contact distance. It is important to note that the minimum distance from an ES to a LEO satellite, $\min(r_{E,S})$, varies from one contact to another, as well as $\max(r_{E,S})$ does.

Differences between the Earth’s rotation rate and LEO orbiting velocities cause an always-varying link length (as seen from a fixed ES), and then, an always-varying elevation angle.

An important relation that needs to be accounted for the elevation angle, θ , and the link length, $r_{S,E}$ is given by the implication that when the angle is minimum, the $r_{S,E}$ distance is maximum, i.e.,

$$\theta \rightarrow \min(\theta) \iff r_{S,E} \rightarrow \max(r_{S,E}), \tag{2}$$

similarly

$$\theta \rightarrow \max(\theta) \iff r_{S,E} \rightarrow \min(r_{S,E}); \tag{3}$$

where the maximum link length, $\max(r_{S,E})$, occurs at some value of θ such that $\min(\theta) < \theta \leq 90^\circ$; and $\min(r_{S,E})$ occurs at some value of $\theta \geq 0^\circ$ lower than θ_{max} . The implications in (2) indicate that when values of θ diminish, $r_{S,E}$ increases; similarly, in (3), when values of θ increase then $r_{S,E}$ decreases.

As a satellite moves away from an ES, $r_{S,E}$ and the free-space path loss, L_{FS} , increases. Longer paths occur for lower values of θ , then, the atmospheric attenuation, A_{Atm} , increases for larger paths (assuming similar atmospheric conditions for different link paths). On the other hand, when θ takes values close to 90° , $r_{S,E}$ will be at its minimum, and so does A_{Atm} . Then, low elevation angles cause a greater L_{FS} , and more atmospheric attenuation, A_{atm} (assuming that the atmospheric conditions are approximately the same for two distinct paths).

For LEO it is important to consider link interference, I , usually addressed as noise in link-budget calculations, and also dependent on the elevation angle as mentioned in [13]. Furthermore, low values of θ are also associated in practice with non-line-of-sight (NLOS) conditions, increasing ground interference [14], and increasing multipath fading in the land mobile satellite (LMS) channel [15–17].

There are several models available in the literature to characterize the received signal from satellite systems. Most of these works have been elaborated for the LMS channel, which describes the received signal at a land-moving ES; nonetheless, most of those works focus on GEO systems. Extensive reviews for the LMS channel can be found at [16,18,19].

Among the available channel models for LMS systems, a few of them focus on characterizations for LEO and non-GEO (NGEO) satellites; but, as noted by [4,20], those are few and there are still many challenges. Most of channels for NGEO systems have been developed based on previous models for GEO satellites, specially on well-known models, such as those by Loo [21] and Lutz [22].

Even though the Loo and Lutz models were not originally intended for LEO satellites, those were later used as a base for much of the non-geosynchronous (NGSO) channel models. The Loo channel assumes that the complex envelope of the received signal, r_T , contains a LOS, r_D , and a multipath component, r_M , which in its phasor notation can be represented as

$$r_T \exp(j\phi_T) = r_D \exp(j\phi_D) + r_M \exp(j\phi_M) \tag{4}$$

where ϕ_T , ϕ_D , and ϕ_M indicate the phase of the total received signal, of the direct or LOS component, and of the multipath component, respectively.

The channel developed by Lutz [22] models a varying received signal affected by different levels of shadowing. This channel is characterized by a Markov chain with a state corresponding to light shadowing, G , and another corresponding to deep shadowing conditions B . Figure 4 illustrates the Lutz channel.

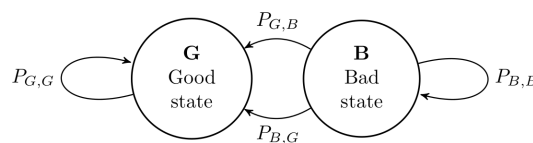


Figure 4. First order Markov chain illustrating the channel model developed by Lutz [22].

The Loo channel [21] was adapted by Corazza and Vatalaro [3] to formulate one of the best-known channel models for LEO satellites; similarly, it was modified by Abdi et al. [23], to achieve straightforward analytical expressions for the first and second order statistics of the received signal based on the Nakagami distribution. However, current models for GEO and NGEO systems have recognized the limitations of a single distribution and a single state to describe the received signal, and multistate models with different distributions at each state have become popular.

Channel models for LEO with multiple states as in [22] have been developed containing the same kind of distribution at each state. For example, a combination of the Lutz and Loo models was implemented for NGSO by Perez-Fontan et al. [24], focusing on time series generation. This model used a three-state Markov chain, as shown in Figure 5, to indicate different levels of shadowing; the first state, S_1 , indicates deep shadow; the second, S_2 , indicates moderate shadowing; and the third state, S_3 , indicates line-of-sight (LOS) conditions. Each state describes the received signal according to a Loo distribution with a different Loo triplet, α, ψ, MP ; and a different Markov chain for distinct elevation angle values. The so-called Loo triplet, which includes the mean of the direct signal amplitude, α , the standard deviation of the direct signal amplitude, ψ , and the multipath power, MP , is the set of parameters required by the Loo distribution.

Figure 6 shows two Loo distributions to characterize the satellite channel at two elevation angles; the CDF's were computed assuming presence of a LOS component, and a multipath power component very close to the LOS level. The Loo distributions in Figure 6 can be understood as two of the states of Figure 5 at different elevation angles; e.g., a state transition from S_{3,θ_1} to S_{3,θ_2} .

In addition to the shadowing level at a receiver environment, which is mainly determined by natural and human made objects at the surroundings of the ES, the received

signal level will be changing according to the elevation angle value. For LEO satellites, the elevation angle will change rapidly, and with a different rate at every contact.

As observed in Figure 6, the Loo CDF curves of the received signal rely on the elevation angle value since those depend on the LOS component of the received signal, α . Then, in order to predict different curves we need to know the expected value and measures of dispersion of the elevation angle.

Even though we illustrate the received signal through the well-known Loo model in Figure 6, there are more LEO channel models depending on a line-of-sight component, and thus, directly depending on the elevation angle. The, elevation angle characterization proposed in this article can be a valuable tool to determine CDF curves of the received signal, based on the first and second order order statistics of the elevation angle. For example, to determine the expected CDF of the Loo model based on the elevation angle expected value, and determine how far apart other curves will be based on the measures of dispersion of the elevation angle.

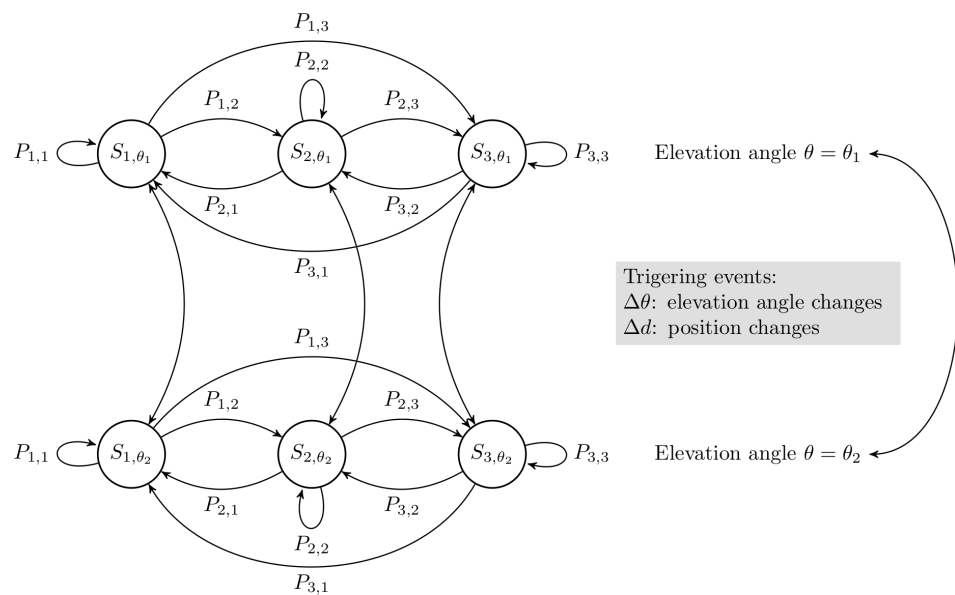


Figure 5. Generalization of a three-state channel model as proposed by [24] considering state transitions based on elevation angle changes.

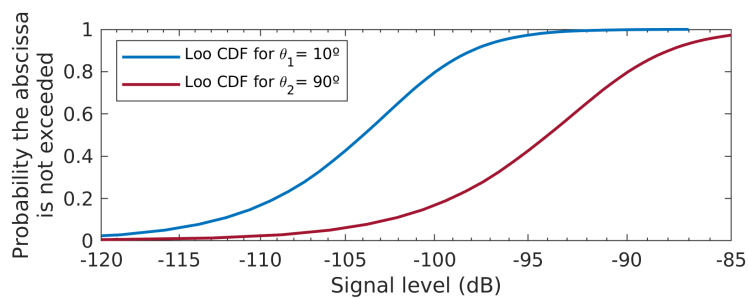


Figure 6. Loo CDF of the received signal for two elevation angle values. The Loo triplet for $\theta_1 = 10^\circ$ is $\alpha = -105$ dB, $\psi = 5$ dB, and $MP = -108$ dB; and $\alpha = -95$ dB, $\psi = 5$ dB, and $MP = -98$ dB for $\theta_2 = 90^\circ$.

2.3. Analytical Characterization of the Elevation Angle

The elevation angle was analytically characterized in [2] through its probability density function (PDF), f_Θ , which is defined as a marginal distribution from the joint PDF of Θ and the maximum value of the elevation angle, Θ_{max} , as follows

$$f_\Theta(\theta) = \int_\theta^{\theta_M} f_{\Theta, \Theta_{max}}(\theta, \theta_{max}) d\theta_{max} \tag{5}$$

where $f_{\Theta, \Theta_{max}}$ is given by

$$f_{\Theta, \Theta_{max}}(\theta, \theta_{max}) = f_{\Theta | \Theta_{max}}(\theta | \theta_{max}) f_{\Theta_{max}}(\theta_{max}) \tag{6}$$

or equivalently

$$f_{\Theta, \Theta_{max}}(\theta, \theta_{max}) = \frac{G(\theta) \sin \gamma(\theta)}{\sqrt{\cos^2 \gamma(\theta_{max}) - \cos^2 \gamma(\theta)}} \cdot \frac{f_{\Theta_{max}}(\theta_{max})}{\int_{\theta_{min}}^{\theta_M} f_{\Theta_{max}}(x) \cos^{-1} \left(\frac{\cos \gamma(\theta_{min})}{\cos \gamma(x)} \right) dx} \tag{7}$$

The integral dividing the right hand term is a constant, say C_1 , then, (7) can be rewritten as

$$f_{\Theta, \Theta_{max}}(\theta, \theta_{max}) = \frac{f_{\Theta_{max}}(\theta_{max}) G(\theta) \sin \gamma(\theta)}{C_1 \sqrt{\cos^2 \gamma(\theta_{max}) - \cos^2 \gamma(\theta)}} \tag{8}$$

and the auxiliary functions $\gamma(\cdot)$ and $G(\cdot)$ require an extra parameter a defined as $a = r_E / r_S$, where $r_E = 6378$ km is the radius of the Earth; and $r_S = r_E + h$ depends on the altitude h (from the Earth’s surface) of the circular LEO orbit in kilometers. The functions $\gamma(\cdot)$ and $G(\cdot)$ are defined as follows

$$\gamma(\theta) = \cos^{-1}(\alpha \cos \theta) - \theta \tag{9}$$

$$G(\theta) = \frac{1 + \alpha^2 - 2\alpha \cos \gamma(\theta)}{1 - \alpha \cos \gamma(\theta)} \tag{10}$$

The term $f_{\Theta_{max}}(\theta_{max})$ is defined as follows

$$f_{\Theta_{max}}(\theta_{max}) = \frac{G(\theta_{max})}{K_2} \cdot f_{\Phi}(\phi_0 - \gamma(\theta_{max})), \quad \text{for } \theta_{min} \leq \theta_{max} < \theta_c \tag{11}$$

$$f_{\Theta_{max}}(\theta_{max}) = \frac{G(\theta_{max})}{K_2} \cdot [f_{\Phi}(\phi_0 - \gamma(\theta_{max})) + f_{\Phi}(\phi_0 + \gamma(\theta_{max}))], \quad \text{for } \theta_c < \theta_{max} < \theta_M \tag{12}$$

where $f_{\Phi}(\phi)$ is defined from the orbital inclination i ; and ES latitude, ϕ , as follows

$$f_{\Phi}(\phi) = \frac{\cos \phi}{\pi \sqrt{\sin^2 i - \sin^2 \phi}}, \quad \text{for } |\phi| < i \tag{13}$$

and $\theta_M = \pi/2$, and K_2 is given by

$$K_2 = \frac{1}{2} - \frac{1}{\pi} \sin^{-1} \left(\frac{\sin(\phi + \gamma(\theta_{min}))}{\sin(i)} \right) \tag{14}$$

where θ_{min} is the minimum elevation angle that will be considered and is in the range $0^\circ < \theta_{min} < 90^\circ$.

Although results shown in [2] are highly accurate with respect to the actual elevation angle PDF, the analytical expression f_{Θ} is cumbersome to obtain and evaluate. Furthermore, analytical expressions for second or higher order statistics, are a missing result in the literature to the best of our knowledge.

3. Methodology for the Elevation Angle Characterization

In this section, we describe the procedure to characterize the elevation angle behavior through a random variable in a manageable analytical expression. Also, we include a

procedure to obtain useful expressions of the elevation angle, such as measures of central tendency and dispersion.

The elevation angle characterization for different LEO orbit's configuration will help to predict which orbits are more convenient for a particular ES location. In addition, the measures of central tendency and dispersion will help to choose suitable orbits based on the expected elevation angle, and to calculate the link attenuation based on the distribution of the elevation angle, and on its expected value and variance.

3.1. Simulations Configuration

Simulations were performed for a LEO satellite with characteristics mentioned in Table 1, and for circular orbit configurations listed in Table 2. The LEO region goes from a few hundred kilometers above the Earth's surface up to 2000 km; but the performed simulations and methodology cover just the upper part of this region since orbit perturbations effects are much lower at those altitudes than at orbital heights closer to the surface, and facilitates operation for longer periods of time without a complex propulsion system.

Table 1. Satellite characteristics for the ephemeris generation.

Dry Mass	Drag Area	Solar Radiation Pressure Area
5 kg	1 m ²	1 m ²

Three initial values of orbital parameters not included in Table 2 are right ascension of the ascending node, Ω , argument of perigee, ω , and true anomaly, ν , which were all set to zero. From those simulations, ephemeris files with the satellite position and velocity in five-second steps were generated. Then, ES's were placed (simulated) at 18 different and arbitrarily chosen locations listed in Table 3. Finally, time series of the observed elevation angle from the ES to the satellite were calculated for each ground location using the previous generated ephemeris files and geometrical relations as in (1).

The orbital mechanical equations required to calculate the position and velocity of the satellite as a function of time, were solved using an open source program developed and maintained by the NASA, GMAT [25]. The time series for the elevation angle discussed in this paper can be generated in GMAT using the data of Tables 1–3; also, these can be generated using other software, for example STK as in [2]. The time series mentioned in this paper were generated by the authors specially for this work, and are available at [26].

Table 2. Orbit characteristics for the ephemeris generation.

	Semi-Major Axis, a	Orbit Inclinations, i
1	7378 km	20°, 25°, ..., 85°
2	7578 km	20°, 25°, ..., 85°
3	7778 km	20°, 25°, ..., 85°
4	7978 km	20°, 25°, ..., 85°
5	8178 km	20°, 25°, ..., 85°
6	8378 km	20°, 25°, ..., 85°

Table 3. ES locations for the performed simulations specified through their latitude, ϕ , and longitude, λ .

	Latitude	Longitude	Latitude	Longitude
ES ₁	0°	276.7121°	ES ₁₀	45°
ES ₂	5°	276.7121°	ES ₁₁	50°
ES ₃	10°	276.7121°	ES ₁₂	55°
ES ₄	15°	267.7121°	ES ₁₃	60°
ES ₅	20°	276.7121°	ES ₁₄	65°
ES ₆	25°	261.7121°	ES ₁₅	70°
ES ₇	30°	259.7121°	ES ₁₆	75°
ES ₈	35°	259.7121°	ES ₁₇	80°
ES ₉	40°	259.7121°	ES ₁₈	-85°

3.2. Elevation Angle Time Series Analysis

Each elevation angle data set (obtained from the simulations) was individually analyzed to observe its statistical values of interest (mean, median, standard deviation, quantiles). Those time series were fitted to several distributions using the maximum likelihood estimation method. The goodness of fit of the proposed distributions was evaluated for each elevation angle time series using the Kolmogorov-Smirnov test, and it was observed a better performance of the gamma distribution, $Gamma(a, b)$, for most of the data sets. Other distributions that showed good fit based on the Kolmogorov-Smirnov test were the beta, $B(a, b)$, and Weibull, $Weib(a, b)$. Figure 7 shows the values of θ as well as the PDF and CDF for one elevation angle time series, $\theta(t)$ using the proposed distributions. Figure 8 shows the Kolmogorov-Smirnov statistic, often indicated as D , for the time series obtained for different altitudes. The Kolmogorov-Smirnov statistic is an indicator of the maximum distance between the actual time series distribution and the proposed gamma distribution. A low value of the Kolmogorov-Smirnov is often desirable to indicate a better goodness-of-fit.

The gamma PDF, $f_{\Theta}(\theta)$, and CDF, $F_{\Theta}(\theta)$, are defined as follows

$$f_{\Theta}(\theta) = \frac{1}{b^a \Gamma(a)} \theta^{a-1} \exp(-\theta/b), \tag{15}$$

and

$$F_{\Theta}(\theta) = \frac{1}{\Gamma(a)} \gamma\left(a, \frac{\theta}{b}\right), \tag{16}$$

respectively, where $\Gamma(\cdot)$ is the gamma function, $\gamma(\cdot)$ is the incomplete gamma function, a is the shape parameter, and b is the scale parameter. By definition both a and b are greater than zero.

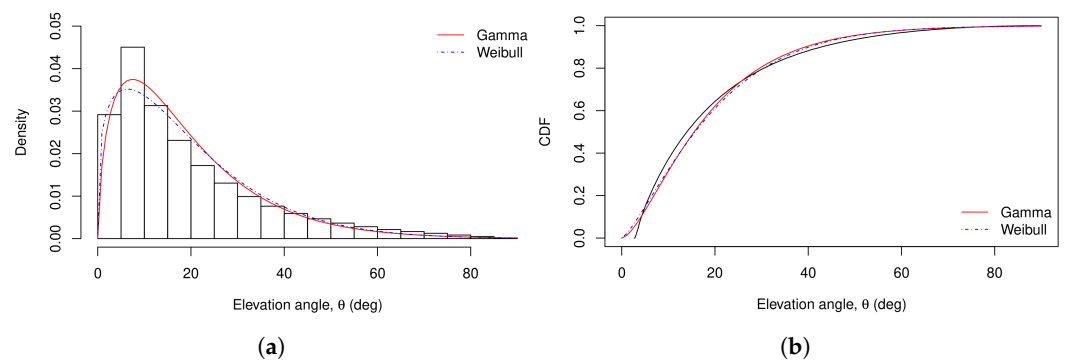


Figure 7. (a) Histogram and (b) theoretical densities for one of the elevation angle data sets obtained from the performed simulations.

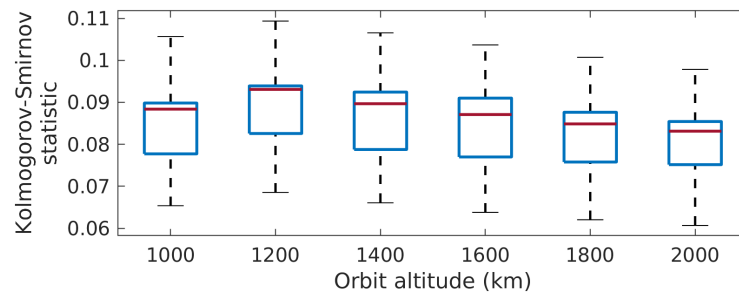


Figure 8. Kolmogorov-Smirnov statistic for the performed simulations at different altitudes.

The shape, a , and scale, b , parameters for the gamma distribution were obtained for each of the elevation angle time series of each ES. Those parameters were organized into several matrix arrays as shown in Table 4, which contains the shape parameter for the simulated orbits as seen from the ES₁, and as in Table 5, which contains the scale parameter also for ES₁.

Table 4. Rate parameter, a , of the gamma distribution to characterize the elevation angle distribution at ES₁, for different altitudes, h , and orbit inclinations, i .

ES ₁	20°	25°	30°	35°	40°	45°	50°	55°	60°	65°	70°	75°	80°	85°
7378 km	1.39	1.50	1.48	1.31	1.30	1.34	1.35	1.35	1.35	1.37	1.37	1.36	1.36	1.37
7578 km	1.62	1.79	1.80	1.65	1.56	1.61	1.62	1.63	1.63	1.64	1.64	1.64	1.64	1.64
7778 km	1.57	1.77	1.82	1.73	1.55	1.61	1.63	1.64	1.64	1.65	1.65	1.66	1.66	1.66
7978 km	1.63	1.74	1.83	1.79	1.62	1.60	1.63	1.65	1.65	1.66	1.66	1.66	1.66	1.67
8178 km	1.70	1.66	1.83	1.82	1.70	1.55	1.63	1.65	1.66	1.67	1.67	1.67	1.70	1.67
8378 km	1.75	1.67	1.82	1.84	1.75	1.58	1.63	1.66	1.67	1.68	1.68	1.68	1.68	1.68

Table 5. Scale parameter of the gamma distribution, $b \times 10^{-2}$, to characterize the elevation angle distribution at ES₁, for different altitudes, h , and orbit inclinations, i .

ES ₁	20°	25°	30°	35°	40°	45°	50°	55°	60°	65°	70°	75°	80°	85°
7378 km	7.51	8.71	9.34	8.88	8.40	8.42	8.40	8.36	8.34	8.39	8.38	8.35	8.35	8.36
7578 km	7.86	9.13	9.91	9.74	9.05	9.02	8.99	8.97	8.93	8.95	8.94	8.93	8.91	8.91
7778 km	7.45	8.55	9.41	9.56	8.83	8.73	8.70	8.67	8.64	8.66	8.64	8.64	8.63	8.64
7978 km	7.41	8.08	8.98	9.33	8.88	8.48	8.46	8.44	8.40	8.41	8.39	8.39	8.38	8.39
8178 km	7.38	7.59	8.60	9.07	8.88	8.18	8.26	8.24	8.22	8.22	8.20	8.18	8.26	8.18
8378 km	7.34	7.47	8.27	8.82	8.83	8.21	8.09	8.08	8.06	8.05	8.03	8.02	8.00	8.02

3.3. Orbit Coverage

Figure 9a illustrates (without scale) passes of a satellite in each one of the six altitudes and for all the inclinations mentioned in Table 2. This figure also shows dashed lines indicating the ES's latitudes mentioned in Table 3.

In Figure 9a as in Table 2 the orbit inclination parameter, i , for each altitude goes from 20° to 85°, then, this figure can be redrawn as the grid shown in Figure 9b, where the curved lines of Figure 9a are replaced by vertical lines indicating the orbit inclination. Additionally, the ES latitude lines were inverted to start with the lowest value at the top.

From Figure 9a it can be observed that satellites with certain orbit inclination i , reach (in its orbit trajectory) at most the latitude that coincide with the inclination value. For example, a satellite with $i = 20^\circ$ will not be able to pass over and ES located at $\phi = 80^\circ$, since the maximum reached latitude in that orbit will be $\phi \approx i \approx 20^\circ$, then, that satellite will be best suited to provide coverage at ES's located at latitudes $\phi \leq i$ or at most $\phi \approx i$. This coincides with basic knowledge of satellite coverage; whereas polar orbits can cover almost all the globe, lower inclination orbits cover smaller portions of the Earth. Then, we can redraw Figure 9b to have a coverage grid by discarding points corresponding to cases of $\phi_{ES} > i_{SAT}$, this resultant grid is shown in Figure 9c.

From the simulation results obtained for the grid points of Figure 9c, matrices A_h and B_h containing the shape and scale parameters of $f_{\Theta}(\theta)$ and $F_{\Theta}(\theta)$ can be defined as follows

$$A_h = \begin{bmatrix} a_{1,1} & a_{1,2} & a_{1,3} & \dots & a_{1,14} \\ a_{2,1} & a_{2,2} & a_{2,3} & \ddots & a_{2,14} \\ a_{3,1} & a_{3,2} & a_{3,3} & \ddots & \vdots \\ a_{4,1} & a_{4,2} & a_{4,3} & \ddots & \vdots \\ a_{5,1} & a_{5,2} & a_{5,3} & \ddots & \vdots \\ NaN & a_{6,2} & a_{6,3} & \ddots & \vdots \\ NaN & NaN & a_{7,3} & \ddots & \vdots \\ \vdots & \vdots & \vdots & \ddots & \vdots \\ NaN & NaN & NaN & \dots & a_{18,14} \end{bmatrix}_{18 \times 14}, \quad B_h = \begin{bmatrix} b_{1,1} & b_{1,2} & b_{1,3} & \dots & b_{1,14} \\ b_{2,1} & b_{2,2} & b_{2,3} & \ddots & b_{2,14} \\ b_{3,1} & b_{3,2} & b_{3,3} & \ddots & \vdots \\ b_{4,1} & b_{4,2} & b_{4,3} & \ddots & \vdots \\ b_{5,1} & b_{5,2} & b_{5,3} & \ddots & \vdots \\ NaN & b_{6,2} & b_{6,3} & \ddots & \vdots \\ NaN & NaN & b_{7,3} & \ddots & \vdots \\ \vdots & \vdots & \vdots & \ddots & \vdots \\ NaN & NaN & NaN & \dots & b_{18,14} \end{bmatrix}_{18 \times 14}, \quad (17)$$

where NaN's are placed for the case $\phi_{ES} > i_{SAT}$, and $h \in h_s$ corresponds to the simulation altitudes set defined in Table 2 as

$$h_s = \{1000 \text{ km}, 1200 \text{ km}, \dots, 2000 \text{ km}\}. \quad (18)$$

Tables A1–A6 in Appendix B, show the shape and scale parameters obtained from simulations with configurations shown in Tables 1–3. From those values, matrices A_h and B_h can be constructed, and linear interpolation can be applied to those in order to obtain shape and scale parameters for different orbit inclinations, ES's latitudes, and altitudes that were not simulated, but are in the range of h_s, i_s, ϕ_s .

3.4. Reducing the Shape and Rate Matrices

From the grid of Figure 9c, an array as shown in Figure 9d can be created for each simulated orbit altitude. Figure 9d shows the diagonal numbers of a rectangular matrix D_h defined as

$$D_h = \begin{bmatrix} d_0 & d_1 & d_2 & \dots & d_{13} \\ d_{-1} & d_0 & d_1 & \ddots & d_{12} \\ d_{-2} & d_{-1} & d_0 & \ddots & \vdots \\ d_{-3} & d_{-2} & d_{-1} & \ddots & \vdots \\ d_{-4} & d_{-3} & d_{-2} & \ddots & \vdots \\ NaN & d_{-4} & d_{-3} & \ddots & \vdots \\ NaN & NaN & d_{-4} & \ddots & \vdots \\ \vdots & \vdots & \vdots & \ddots & \vdots \\ NaN & NaN & NaN & \dots & d_{-4} \end{bmatrix}_{18 \times 14}, \quad (19)$$

for each altitude $h \in h_s$, with NaN's are placed for cases where $\phi_{ES} > i_{SAT}$.

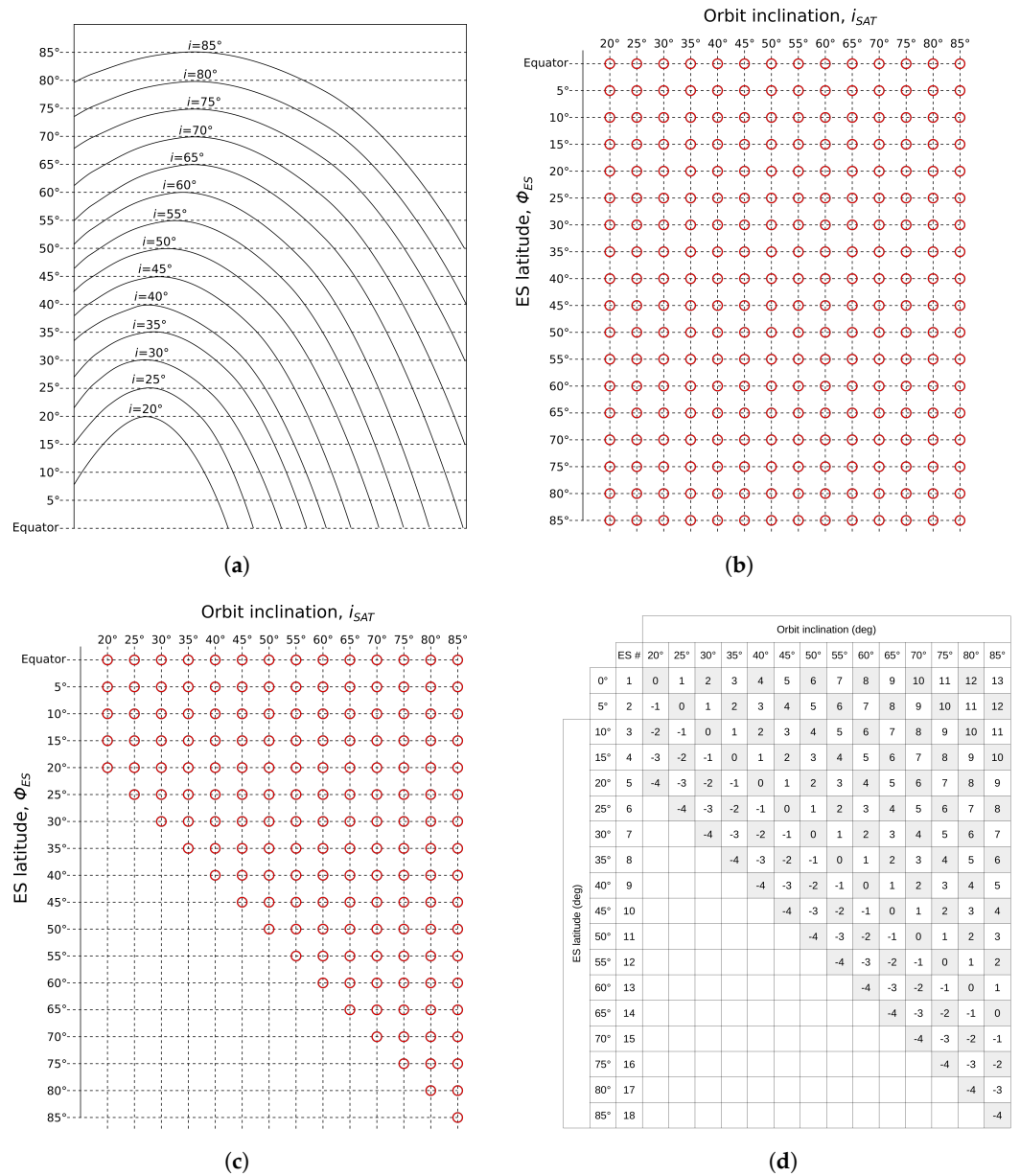


Figure 9. Simulated orbits: (a) Model without scale illustrating satellite passes at different orbit inclinations, i , over different ES's latitudes. (b) Simulated orbit inclinations and ES's latitudes as points in a grid. (c) Reduction of the grid showing in each column the ES's below the simulated orbit inclinations. (d) Simulated points as diagonal elements within a matrix.

3.5. PDF and CDF of the Elevation Angle

In addition to h_s , we can define two additional sets containing the orbit inclinations (as in Table 2) and ES's latitudes (as in Table 3) at which simulations were performed, as

$$i_s = \{20^\circ, 25^\circ, \dots, 85^\circ\} \quad (20)$$

and

$$\phi_s = \{0^\circ, 5^\circ, \dots, 85^\circ\}, \quad (21)$$

respectively.

Depending on the input values of ϕ_k , h_k , and i_k , if those are part of the previously defined sets (i_s, h_s, ϕ_s) eight cases can arise as follows:

- Case 1. $i_k \in i_s$ and $\phi_k \in \phi_s$ and $h_k \in h_s$

- Case 2. $i_k \in i_s$ and $\phi_k \in \phi_s$ and $h_k \notin h_s$
- Case 3. $i_k \in i_s$ and $\phi_k \notin \phi_s$ and $h_k \in h_s$
- Case 4. $i_k \in i_s$ and $\phi_k \notin \phi_s$ and $h_k \notin h_s$
- Case 5. $i_k \notin i_s$ and $\phi_k \in \phi_s$ and $h_k \in h_s$
- Case 6. $i_k \notin i_s$ and $\phi_k \in \phi_s$ and $h_k \notin h_s$
- Case 7. $i_k \notin i_s$ and $\phi_k \notin \phi_s$ and $h_k \in h_s$
- Case 8. $i_k \notin i_s$ and $\phi_k \notin \phi_s$ and $h_k \notin h_s$

Case 1 occurs when all the input values ϕ_k , i_k and h_k are contained in ϕ_s , i_s , and h_s , respectively; and Case 8 occurs when none of ϕ_k , i_k and h_k parameters coincide with previously simulated values. Cases 2 to 7 occur when at least one of the input values (any of ϕ_k , i_k , and h_k) coincides with a value within its corresponding sets ϕ_s , i_s and h_s . Those cases illustrate all possible scenarios, ranging from not-required interpolation to interpolation inside a four-point mesh.

We can represent the ES latitude, ϕ_k , orbit inclination, i_k , or both (for which we want to determine their PDF) as a query point between two-known points, inside a three-point mesh, or inside a four-point mesh. Then we can use an interpolation method, such as those proposed in Appendix C, to find an appropriate value for the gamma distribution parameters at that query coordinates. In addition to those proposed in Appendix C, more interpolation methods are widely available in the literature.

3.6. First and Second Order Statistics of $f_{\Theta}(\theta)$

The elevation angle expected value can be calculated from (15) as

$$E[\Theta] = \int_{\theta} \theta f_{\Theta}(\theta) d\theta, \tag{22}$$

Nonetheless, sometimes a satellite link requires to operate above a minimum value of θ , θ_{min} , then, elevation angle values below θ_{min} are not of interest. Recent satellite systems operating above the Ku band consider θ_{min} values above some tens of degrees, e.g., the Starlink constellation considered a $\theta_{min} = 40^\circ$ as mentioned in [27]. We can obtain the conditional expected value for values above θ_{min} using conditional probability as follows

$$E[\Theta | \Theta \geq \theta_{min}] = \int_{\theta} \theta f_{\Theta}(\theta | \theta \geq \theta_{min}) d\theta, \tag{23}$$

which can be rewritten as in [28] as

$$E[\Theta | \Theta \geq \theta_{min}] = \frac{\int_{\theta_{min}}^{\theta_{max}} \theta f_{\Theta}(\theta) d\theta}{F_{\Theta}(\theta_{max}) - F_{\Theta}(\theta_{min})}, \tag{24}$$

The variance of Θ , is obtained as follows

$$\text{Var}[\Theta | \Theta \geq \theta_{min}] = E[\Theta^2 | \Theta \geq \theta_{min}] - E[\Theta | \Theta \geq \theta_{min}]^2, \tag{25}$$

And the standard deviation of Θ is then defined as

$$\text{SD}[\Theta | \Theta \geq \theta_{min}] = \text{Var}[\Theta | \Theta \geq \theta_{min}]^{1/2} \tag{26}$$

3.7. Choosing Orbits to Maximize Mean Value of θ

It is possible to choose an orbit configuration to maximize the elevation angle expected value, $E[\Theta|\Theta \geq \theta_{min}]$, for given ranges of ϕ , h , and i . The problem can be stated as

$$\begin{aligned} \max_{i,\phi,h} \quad & E[\Theta|\Theta \geq \theta_{min}] \\ \text{s.t.} \quad & i_1 \leq i \leq i_2 \\ & \phi_1 \leq \phi \leq \phi_2 \\ & h_1 \leq h \leq h_2 \end{aligned} \tag{27}$$

where $i_1 \leq i_2$, $\phi_1 \leq \phi_2$, and $h_1 \leq h_2$. This problem can be solved by optimization methods or using computational tools to perform an iterative evaluation within a `for` or `while` cycle.

Reduction of the Elements in the Diagonals

It was found that functions $f_{\Theta}(\theta)$ and $F_{\Theta}(\theta)$ were very similar for some diagonals, d shown in Figure 9d. Then, from the diagonals as shown in Figure 9d, we propose a reduction first, by obtaining the expected value $E[\cdot]$ of each diagonal, d_l , (note the use of subindex $l \in \{-4, -3, \dots, 13\}$ as an indicator of the diagonal number) as $E[d_l]$. Then, (19) can be rewritten as the following row vector

$$E[\mathbf{D}_h] = [E[d_{-4}], E[d_{-3}], \dots, E[d_{13}]]_{1 \times 18} \tag{28}$$

where the diagonals with just *NaN*'s elements are omitted.

From observation, we find that some adjacent elements in $E[\mathbf{D}_h]$ are approximately equal, then, we reduced $E[\mathbf{D}_h]$ by taking the mean value of adjacent similar values according to

$$\frac{1}{|L-l|} \sum_l^L E[d_l], \quad L > l \tag{29}$$

where l , and L are, respectively, the lower and upper diagonal numbers for the interval in which the values $E[d_l], E[d_{l+1}], \dots, E[d_L]$ were observed approximately the same (with a maximum-distance criteria between the fitted curves of 5%). After this reduction $E[\mathbf{D}_h]$ ends as a row vector with only four elements, and we call this vector \mathbf{p}_h for $h \in h_s$. This procedure can be repeated for each altitude in h_s , and after grouping all the row vectors \mathbf{p}_h for all simulated altitudes h we arrive to the matrix \mathbf{P} given by

$$\mathbf{P} = \begin{bmatrix} \mathbf{p}_{1000\text{km}} \\ \mathbf{p}_{1200\text{km}} \\ \mathbf{p}_{1400\text{km}} \\ \mathbf{p}_{1600\text{km}} \\ \mathbf{p}_{1800\text{km}} \\ \mathbf{p}_{2000\text{km}} \end{bmatrix} = \begin{bmatrix} p_{1,1} & p_{1,2} & p_{1,3} & p_{1,4} \\ p_{2,1} & p_{2,2} & p_{2,3} & p_{2,4} \\ p_{3,1} & p_{3,2} & p_{3,3} & p_{3,4} \\ p_{4,1} & p_{4,2} & p_{4,3} & p_{4,4} \\ p_{5,1} & p_{5,2} & p_{5,3} & p_{5,4} \\ p_{6,1} & p_{6,2} & p_{6,3} & p_{6,4} \end{bmatrix} \tag{30}$$

Matrix \mathbf{P} will be called \mathbf{P}_a if it contains the shape parameters, a , for $f_{\Theta}(\theta)$, and \mathbf{P}_b if it contains the scale parameter, b , for $f_{\Theta}(\theta)$.

From matrices \mathbf{P}_a and \mathbf{P}_b , it is possible to recover any of the points of \mathbf{A}_h and \mathbf{B}_h and then estimate the CDF for a query orbit altitude h_k , orbit inclination, i_k , and ES's latitude, ϕ_k . However, we observed that some $F_{\Theta}(\theta)$ curves for high latitudes were not fitting very well after the reduction from matrices \mathbf{A}_h and \mathbf{B}_h to \mathbf{P}_a and \mathbf{P}_b , then, two weight matrices were obtained through manual tuning to improve the correspondence between \mathbf{P}_a and

A_h , and between P_b and B_h . The weight matrix for the shape parameter, w_a and w_b , is defined as

$$w_a = \begin{bmatrix} w_{a_{1,1}} & w_{a_{1,2}} & w_{a_{1,3}} & \dots & w_{a_{1,14}} \\ w_{a_{2,1}} & w_{a_{2,2}} & w_{a_{2,3}} & \ddots & w_{a_{2,14}} \\ w_{a_{3,1}} & w_{a_{3,2}} & w_{a_{3,3}} & \ddots & \vdots \\ w_{a_{4,1}} & w_{a_{4,2}} & w_{a_{4,3}} & \ddots & \vdots \\ w_{a_{5,1}} & w_{a_{5,2}} & w_{a_{5,3}} & \ddots & \vdots \\ NaN & w_{a_{6,2}} & w_{a_{6,3}} & \ddots & \vdots \\ NaN & NaN & w_{a_{7,3}} & \ddots & \vdots \\ \vdots & \vdots & \vdots & \ddots & \vdots \\ NaN & NaN & NaN & \dots & w_{a_{18,14}} \end{bmatrix}_{18 \times 14}, \quad w_b = \begin{bmatrix} w_{b_{1,1}} & w_{b_{1,2}} & w_{b_{1,3}} & \dots & w_{b_{1,14}} \\ w_{b_{2,1}} & w_{b_{2,2}} & w_{b_{2,3}} & \ddots & w_{b_{2,14}} \\ w_{b_{3,1}} & w_{b_{3,2}} & w_{b_{3,3}} & \ddots & \vdots \\ w_{b_{4,1}} & w_{b_{4,2}} & w_{b_{4,3}} & \ddots & \vdots \\ w_{b_{5,1}} & w_{b_{5,2}} & w_{b_{5,3}} & \ddots & \vdots \\ NaN & w_{b_{6,2}} & w_{b_{6,3}} & \ddots & \vdots \\ NaN & NaN & w_{b_{7,3}} & \ddots & \vdots \\ \vdots & \vdots & \vdots & \ddots & \vdots \\ NaN & NaN & NaN & \dots & w_{b_{18,14}} \end{bmatrix}_{18 \times 14}, \quad (31)$$

Both w_a and w_b are the same for all altitudes, and their numerical values are shown in Appendix B.

4. Results

The shape, a , and rate, b , parameters for matrices P_a and P_b , respectively, are shown in Tables 6 and 7 for the orbit altitudes $h \in h_s$ and for the diagonals as in D_h , (19).

Table 6. Shape parameter, a , for matrix P_a , using the diagonal notation as in (19), and as shown in Figure 9d.

Altitude	(d_{-4}, d_{-2})	Diagonals Range		
		(d_{-1}, d_0)	(d_1, d_2)	(d_3, d_{13})
1000 km	1.470954	1.638425	1.450794	1.488802
1200 km	1.707323	1.935321	1.721572	1.752709
1400 km	1.712923	1.951520	1.746205	1.754760
1600 km	1.723436	1.955254	1.782190	1.757023
1800 km	1.731110	1.952362	1.796549	1.774827
2000 km	1.741450	1.954794	1.836833	1.760709

Table 7. Rate parameter, $b \times 10^{-2}$, for matrix P_b , using the diagonal notation as in (19), and as shown in Figure 9d.

Altitude	(d_{-4}, d_{-2})	Diagonals Range		
		(d_{-1}, d_0)	(d_1, d_2)	(d_3, d_{13})
1000 km	7.037052	9.459459	9.075805	8.805617
1200 km	7.391963	9.840010	9.640436	9.284945
1400 km	7.130587	9.319436	9.412412	8.952740
1600 km	6.943998	8.879456	9.242146	8.693598
1800 km	6.791048	8.510588	9.041604	8.632867
2000 km	6.675182	8.224503	8.941424	8.305444

Figure 10a–c show the PDF obtained from the empirical data and the ones obtained from the parameters listed in Tables 6 and 7. Table 8 shows the shape, a , and scale, b , parameters as well as the first and second order statistics for the $f_{\Theta}(\theta)$ functions of Figure 10a–d.

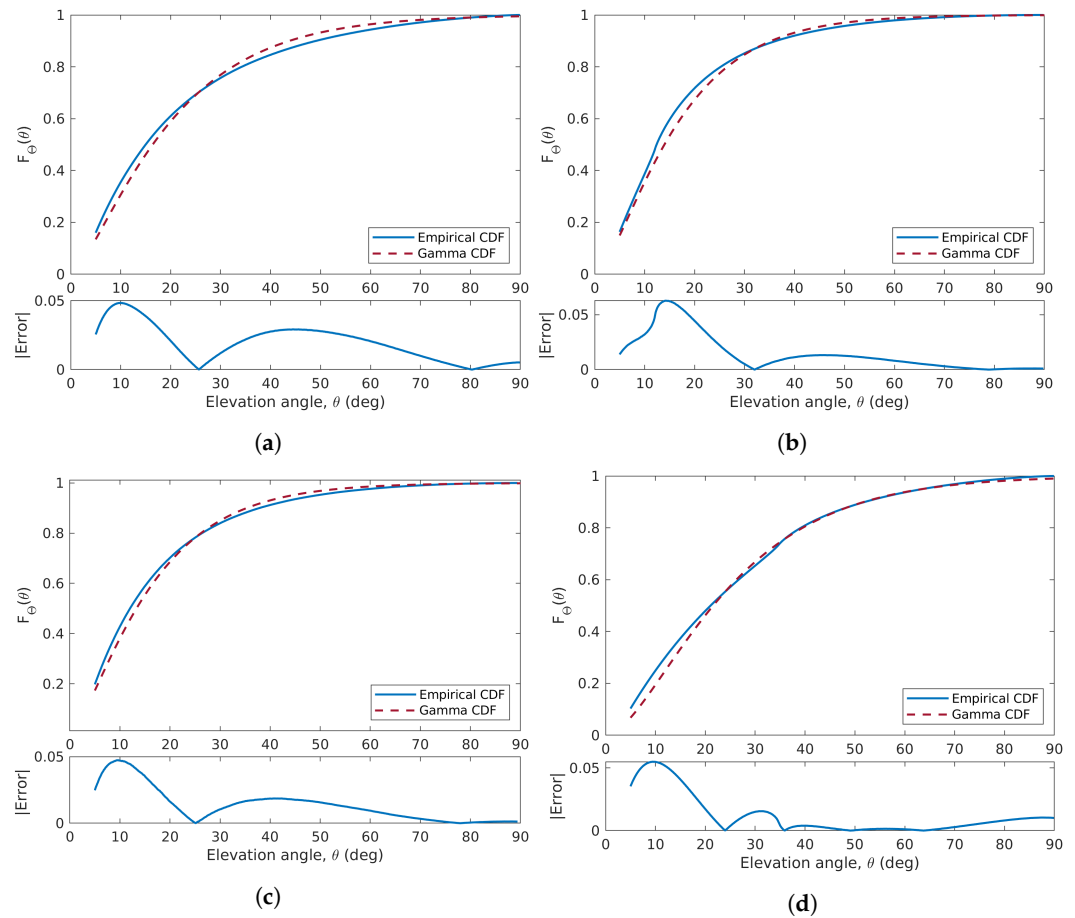


Figure 10. Comparison and error of the empirical and Gamma elevation angle CDF's for different ES latitudes, ϕ_{ES} , orbit inclinations of the satellites, i_{SAT} , and, orbit altitudes, h_k . (a) CDF's for $\phi_{ES} = 30^\circ$ and $i_{SAT} = 30^\circ$ at $h_k = 1000$ km; (b) CDF's for $\phi_{ES} = 45^\circ$ and $i_{SAT} = 65^\circ$ at $h_k = 1000$ km; (c) CDF's for $\phi_{ES} = 20^\circ$ and $i_{SAT} = 75^\circ$ at $h_k = 1000$ km; (d) CDF's for $\phi_{ES} = 85^\circ$ and $i_{SAT} = 85^\circ$ at $h_k = 1000$ km.

Table 8. First and second order statistics of the elevation angle for the same orbit configurations and ES's locations that in Figure 10a–d.

	Empirical Result	Proposed Method's Result	Empirical Result	Proposed Method's Results	Empirical Result	Proposed Method's Results	Empirical Result	Proposed Method's Results
ES latitude, ϕ_{ES}		30°		45°		20°		85°
Orbit inclination, i_{SAT}		30°		65°		75°		85°
Orbit altitude, h_{SAT}		1000 km						
Shape parameter, a	–	1.4710	–	1.6384	–	1.4888	–	1.8387
Rate parameter, $b \times 10^{-2}$	–	7.0371	–	9.4595	–	8.8056	–	7.0371
$E[\Theta > 5^\circ]$	24.55°	23.09°	19.43°	19.74°	20.24°	19.70°	27.70°	26.66°
$SD[\Theta > 5^\circ]$	18.40°	16.86°	14.19°	13.13°	14.94°	13.48°	18.12°	18.90°
$E[\Theta > 15^\circ]$	34.77°	31.13°	29.77°	27.96°	30.55°	28.24°	35.48°	33.23°
$SD[\Theta > 15^\circ]$	17.46°	16.26°	14.24°	12.45°	14.49°	12.93°	16.32°	17.96°
$E[\Theta > 25^\circ]$	44.33°	39.66°	40.12°	37.03°	40.39°	37.38°	42.73°	40.91°
$SD[\Theta > 25^\circ]$	15.93°	15.88°	13.40°	12.05°	13.50°	12.61°	14.79°	17.29°

A case study was developed for a satellite with an altitude of 1500 km, an orbit inclination of 43° , and ES latitude of 22° . Using the numerical results of Tables 6 and 7, a mesh as shown in Figure 11a can be created for altitudes of 1400 km and 1600 km (shape and scale values were obtained for those altitudes and are shown in Tables 6 and 7). Then, using an interpolation method as that described in Appendix C, parameters a and b can be obtained to characterize the elevation angle curve.

The shape and scale parameters for the case study are shown in Table 9. First, parameters for the four-points (as in Figure 11b) are listed for each altitude (1400 km and 1600 km). Then, the resultant parameters obtained from interpolation were computed. Finally, the shape and scale parameters for the query altitude can be obtained using a weighted arithmetic mean where the weights can be obtained from the distance of the query altitude to the closest characterized orbit altitudes. In this case, the distances from the query altitude to the closest characterized altitudes are the same, then we obtained the shape and scale for the query altitude using the arithmetic mean of the shape and scale values at 1400 km and 1600 km.

Both the elevation angle CDF obtained with the proposed methodology and the empirical CDF are shown in Figure 11b. The distance magnitude between those two curves is also shown in Figure 11b and labeled as absolute error ($|\text{Error}|$). The distance (or error) between the gamma CDF and the empirical CDF is very small, and its maximum value is around 0.025 (2.5%).

Table 9. Shape and scale parameters for the elevation angle PDF and CDF for $\phi_{ES} = 22^\circ$ and $i_{SAT} = 43^\circ$ at $h_k = 1500$ km, corresponding to the four-point mesh shown in Figure 11a.

Four-Point Mesh Setup					
	1400	1600		1400	1600
$a(\phi_1, i_1)$	1.9515	1.9552	$b(\phi_1, i_1)$	9.3194×10^{-2}	8.8794×10^{-2}
$a(\phi_1, i_2)$	1.9515	1.9552	$b(\phi_1, i_2)$	9.3194×10^{-2}	8.8794×10^{-2}
$a(\phi_2, i_1)$	1.9515	1.9552	$b(\phi_2, i_1)$	9.3194×10^{-2}	8.8794×10^{-2}
$a(\phi_2, i_2)$	1.7462	1.7822	$b(\phi_2, i_2)$	9.4112×10^{-2}	9.2215×10^{-2}
Obtained parameters from interpolation					
$a(\phi, i)$	1.8776	1.8929	$b(\phi, i)$	9.3529×10^{-2}	9.0025×10^{-2}
$a(\phi, i)$		1.8853	$b(\phi, i)$		9.1777×10^{-2}
Empirical parameters					
$a(\phi, i)$		1.9804	$b(\phi, i)$		9.5987×10^{-2}

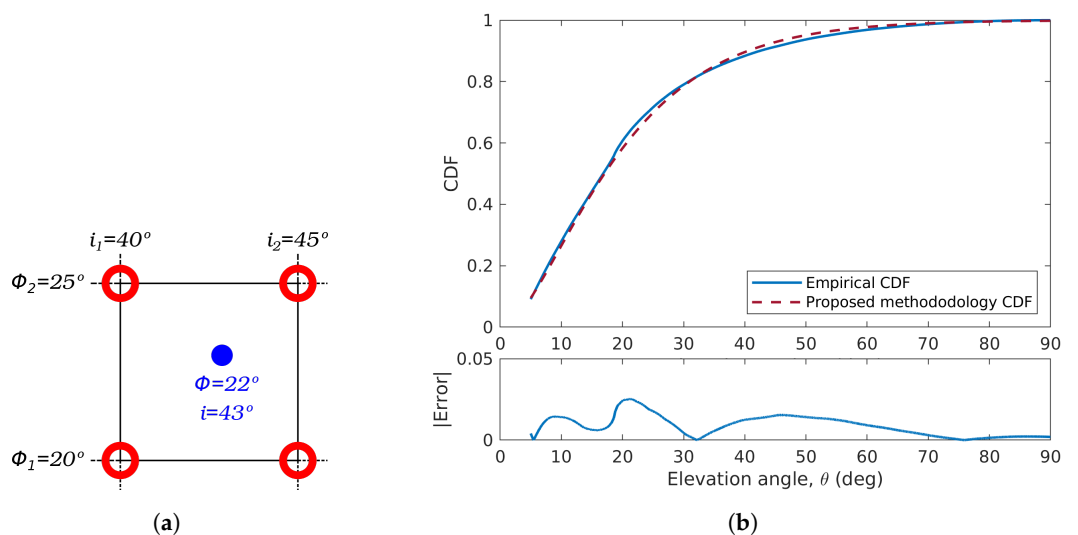


Figure 11. Example case results for $\phi_{ES} = 22^\circ$, $i_{SAT} = 43^\circ$ and $h_k = 1500$ km: (a) four-point mesh to calculate the shape, a , and scale, b parameters of $f_\theta(\theta)$ and (b) empirical CDF vs. CDF obtained with the proposed methodology.

4.1. Results Validity

4.1.1. Effects of the Orbit Configuration in the Elevation Angle Distribution

The Kepler orbital elements were chosen to describe the orbits, those parameters include the semi-major axis, a , eccentricity, e , orbit inclination, i , right ascension of the ascending node, Ω , argument of perigee, ω , and true anomaly, ν . The values of the right ascension of the ascending node, Ω , argument of perigee, ω , and true anomaly, ν , do not affect the statistical properties of the elevation angle, then, those values are not further discussed. Figure 12a,b show the PDF and CDF elevation angle curves observed from the same location for two simulated satellites with different orbit configurations which share the same initial semi-major axis, a , eccentricity, e , and orbit inclination, i ; but, differ in the initial values of the right ascension of the ascending node, Ω , argument of perigee, ω , and of the true anomaly, ν .

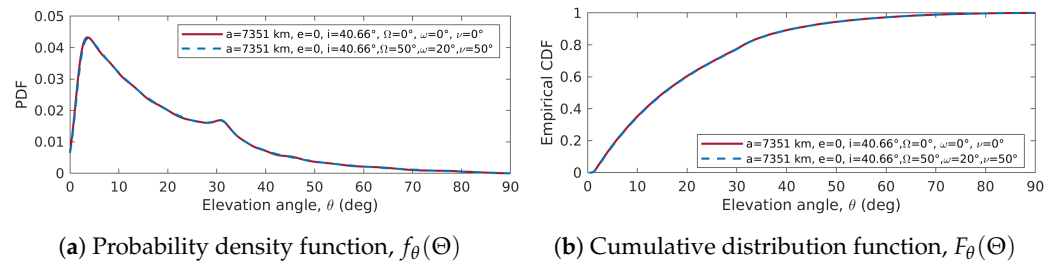


Figure 12. PDF and CDF for two orbit configurations sharing the same altitude, eccentricity, and orbit inclination, but with the remaining orbital parameters being different.

4.1.2. Elevation Angle CDF for Different Longitudes

ES's located at different longitudes share approximately the same elevation angle distribution for the same LEO satellite configuration. The reasoning behind this fact is discussed in [2], and it is illustrated in Figure 13a, which shows the elevation angle PDF for three ES's located at the same latitude, ϕ , but at different longitudes, λ 's. Figure 13a shows that the elevation angle PDF is the same for ES located at different longitudes, λ 's, when they share the same latitude, ϕ , and those are served by satellites with the same orbit configuration (semi-major axis, a , eccentricity, e , and, inclination, i). The PDF's shown in Figure 13a were generated for a satellite with a circular orbit and an inclination of $i = 60^\circ$, and an altitude of $h = 1800$ km; in addition, all ES's were located at the same latitude $\phi = 25^\circ$ N.

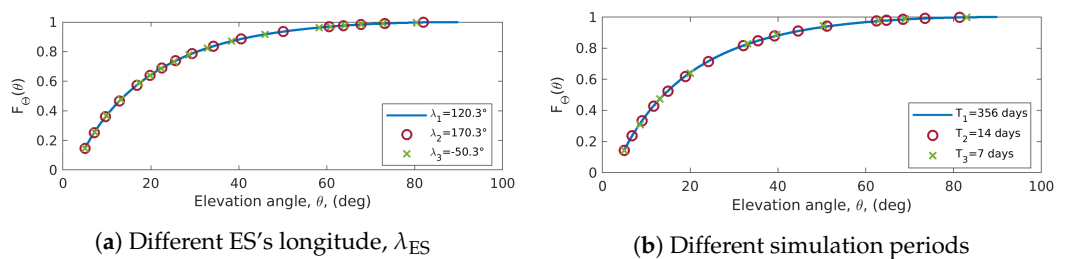


Figure 13. CDF $F_\Theta(\theta)$ for the same orbit configuration and ES latitude but for (a) different ES longitude and (b) different simulation period.

4.1.3. Long Term Validity of $f_\Theta(\theta)$ and $F_\Theta(\theta)$

From a few days $f_\Theta(\theta)$ can be observed very similar compared with the same PDF is a much greater period, e.g., one year. Figure 13b shows the functions $F_\Theta(\theta)$ for three different simulation periods ranging from one week to one year. The CDF curve is almost identical for all the simulation periods. The orbit configuration and ES's location were choose to be the same that for Figure 13a.

4.1.4. Elevation Angle CDF for Different Satellite Characteristics

Simulations for this paper were performed for a satellite with the mass and drag areas listed in Table 1, nonetheless, satellites with different values in those characteristics will share very similar functions $F_{\Theta}(\theta)$. Figure 14 shows the empirical CDF's for two satellites with the same orbital parameters but with different mass and drag areas. For both satellites, the orbit altitude, h , was set to 1800 km and the orbit inclination, i , to 60° , and both ES's were located at 25° N. As shown in Figure 14, variations in the satellite mass and drag area characteristics will have a very little impact in the elevation angle CDF's. For lower altitudes the effect is greater, but not significant enough for the altitudes covered in this paper. Table 10 show the mass and areas for satellites shown in Figure 14.

Table 10. Satellites with different mass and drag area characteristics for additional performed simulations.

	Satellite 1	Satellite 2
Dry mass	5 kg	200 kg
Drag area	1 m ²	10 m ²
Solar radiation pressure area	1 m ²	10 m ²

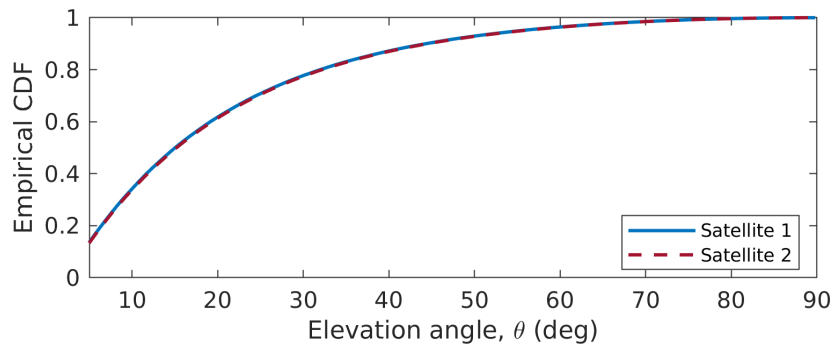


Figure 14. CDF $F_{\Theta}(\theta)$ for different satellite mass and drag area characteristics.

4.2. Error Analysis

The error between the empirical CDF curves of the elevation angle and the ones obtained with the parameters in Tables 6 and 7, was quantified by means of the absolute error, ϵ , and its CDF. Figure A1a–f in Appendix A show the mean absolute error, $\bar{\epsilon}$, between the empirical CDF's for the simulated points of Figure 9c, and for the orbit altitudes $h_k \in h_s$.

The maximum observed mean error for the individual characterizations shown in Appendix A was about 5% ($\bar{\epsilon}_{max} \approx 0.05$) for the worst case. However, the greatest error values were observed to occur at lower elevation angles (below 20° where the link is often unreliable since line-of-sight is harder to find) that are often not considered by satellite communication systems due to greater attenuation.

The absolute errors ϵ were also analyzed through their individual CDF's, showing that most of the errors were below 5%. Figure 15a–d show the CDF's of the absolute error, ϵ , corresponding to Figure 10a–d. In addition, ϵ was analyzed for all the simulated satellite orbits and according to their elevation angle range.

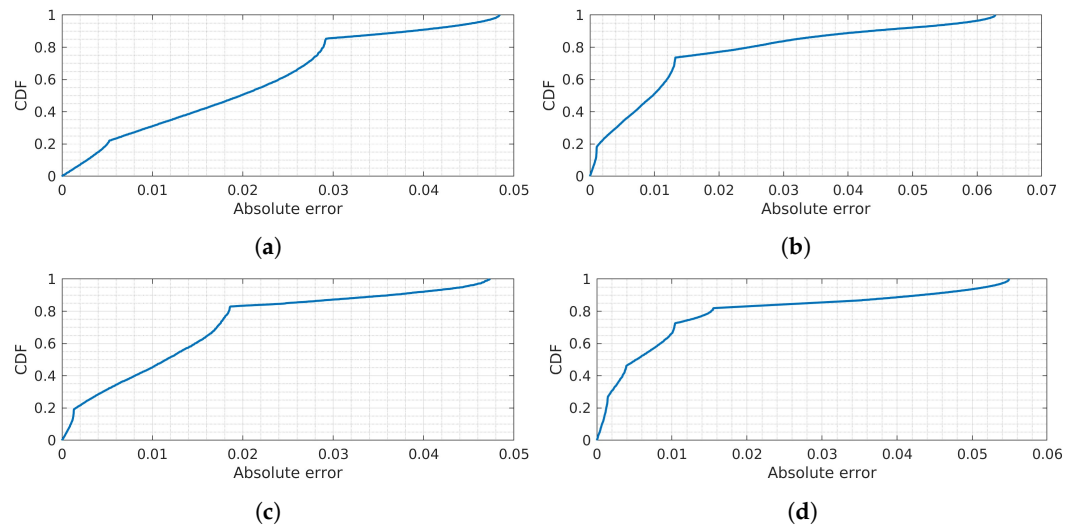


Figure 15. CDF's for the absolute errors at different orbit configurations and ES's as in Figure 10a–d. Absolute error CDF's for: (a) $\phi_{ES} = 30^\circ$ and $i_{SAT} = 30^\circ$ at $h_k = 1000$ km; (b) $\phi_{ES} = 45^\circ$ and $i_{SAT} = 65^\circ$ at $h_k = 1000$ km; (c) $\phi_{ES} = 20^\circ$ and $i_{SAT} = 75^\circ$ at $h_k = 1000$ km; (d) $\phi_{ES} = 85^\circ$ and $i_{SAT} = 85^\circ$ at $h_k = 1000$ km.

The PDF, CDF, and the complementary CDF (CCDF) showing the resultant absolute errors, ϵ , for all the simulations are shown in Figure 16, where it can be observed that around 95% of the values of ϵ are below 0.05. Figure 17 shows the same absolute errors as in Figure 16b, but now expanded and classified by elevation angle range; in this figure, it can be observed that most of the absolute errors are below 5% for all the elevation angle ranges, and that errors' CDF distributions are approximately the same for all the elevation angle ranges. Figure 18 expands the 90th-percentile of the CDF's in Figure 17, showing that in fact, most of the errors are below 2%; the 90th-percentile mean value is shown as a red cross for each boxplot.

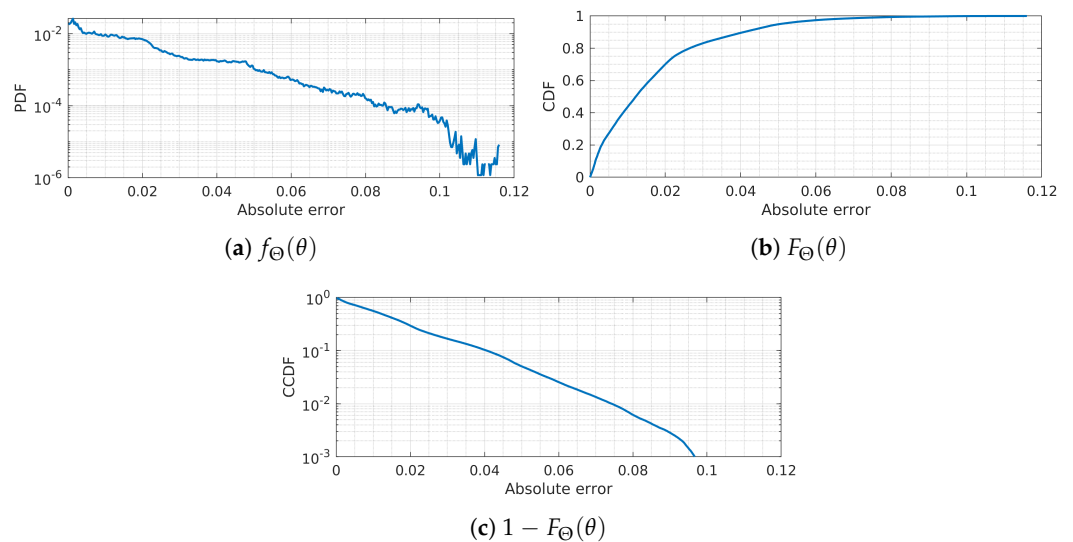


Figure 16. Distribution of the absolute errors behavior of all the performed simulations: (a) PDF, (b) CDF, and (c) CCDF.

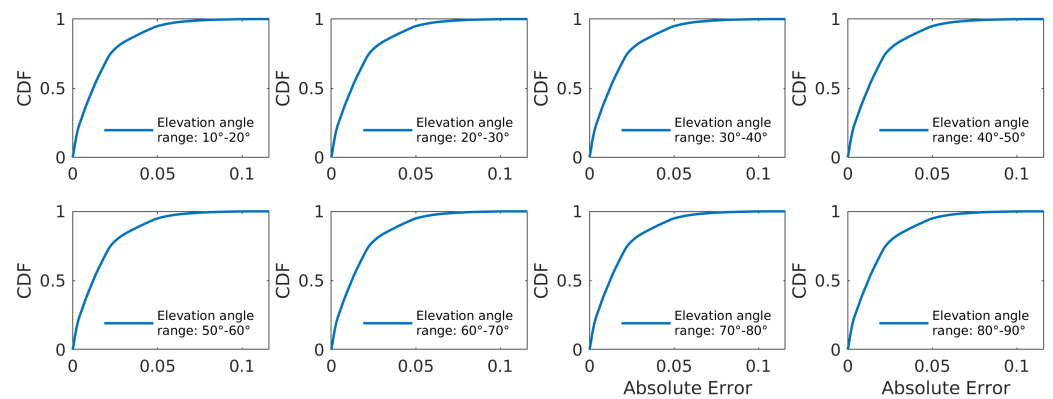


Figure 17. CDF's of the absolute error by elevation angle range for all the simulated orbits and ES's.

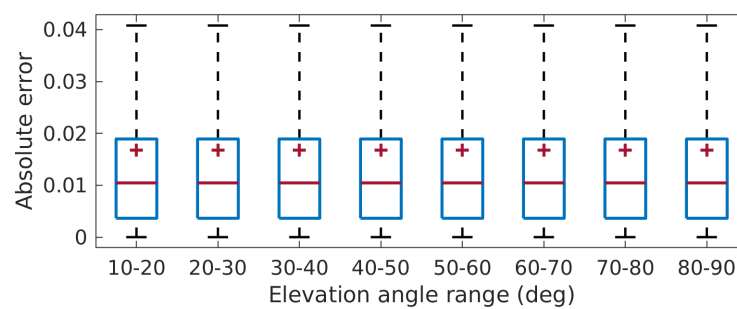


Figure 18. Boxplots of the absolute error by elevation angle range. Simulation results vs proposed methodology.

5. Conclusions

This article demonstrated the feasibility of using a gamma random variable to characterize the elevation angle PDF and CDF. The proposed methodology allowed PDF and CDF calculations of the elevation angle for LEO satellites for altitudes between 1000 km and 2000 km. The characterization of elevation angle through a gamma random variable allowed an easy computation of first and second order statistics, which, to the best of our knowledge, have not been previously addressed in the literature.

The proposed methodology was validated with an error analysis against the empirical CDF's. The results showed that errors are low, with a mean absolute error much below 5% in most of the cases, and with around 95% of the total errors being below 5%.

Furthermore, the proposed methodology allows an easy comparison between multiple orbits in order to determine the most suitable orbital parameters to provide coverage above a minimum elevation angle at a particular latitude.

Author Contributions: Conceptualization, J.M.G.-T. and C.V.-R.; methodology and software, J.M.G.-T.; validation, A.A.-Z. and R.V.-H.; formal analysis, A.A.-Z. and R.V.-H.; investigation, A.A.-Z. and R.V.-H.; writing—original draft preparation, J.M.G.-T.; writing—review and editing, C.V.-R., A.A.-Z. and R.V.-H.; visualization, J.M.G.-T.; supervision, J.M.G.-T., C.V.-R. and A.A.-Z.; project administration, C.V.-R. and R.V.-H. All authors have read and agreed to the published version of the manuscript.

Funding: This research received no external funding.

Institutional Review Board Statement: Not applicable.

Informed Consent Statement: Not applicable.

Data Availability Statement: Not applicable.

Acknowledgments: We would like to acknowledge the support from the Smart Digital Technologies and Infrastructure Research Group, the project “Digital Technologies to Create Adaptive Smart Cities” as part of the Challenge-Based Research Funding Program, and the School of Engineering and Sciences at Tecnológico de Monterrey for providing the means to develop this collaborative work.

Conflicts of Interest: The authors declare no conflict of interest.

Abbreviations

The following abbreviations are used in this manuscript:

- CDF Cumulative distribution function
- CCDF Complementary cumulative distribution function
- ES Earth station
- GEO Geostationary Earth orbit
- LEO Low Earth orbit
- LMS Land mobile satellite
- LOS Line-of-sight
- NGEO Non-Geostationary Earth orbit
- NGSO Non-Geosynchronous orbit
- NLOS Non-line-of-sight
- PDF Probability density function

Appendix A

Figure A1a–f contain the mean error for each elevation angle CDF. Those errors were obtained by comparing the proposed methodology results against the results obtained through simulations. The same format than in Figure 9c,d is applied here; only showing the ES’s located below the satellite orbit inclinations at each column.

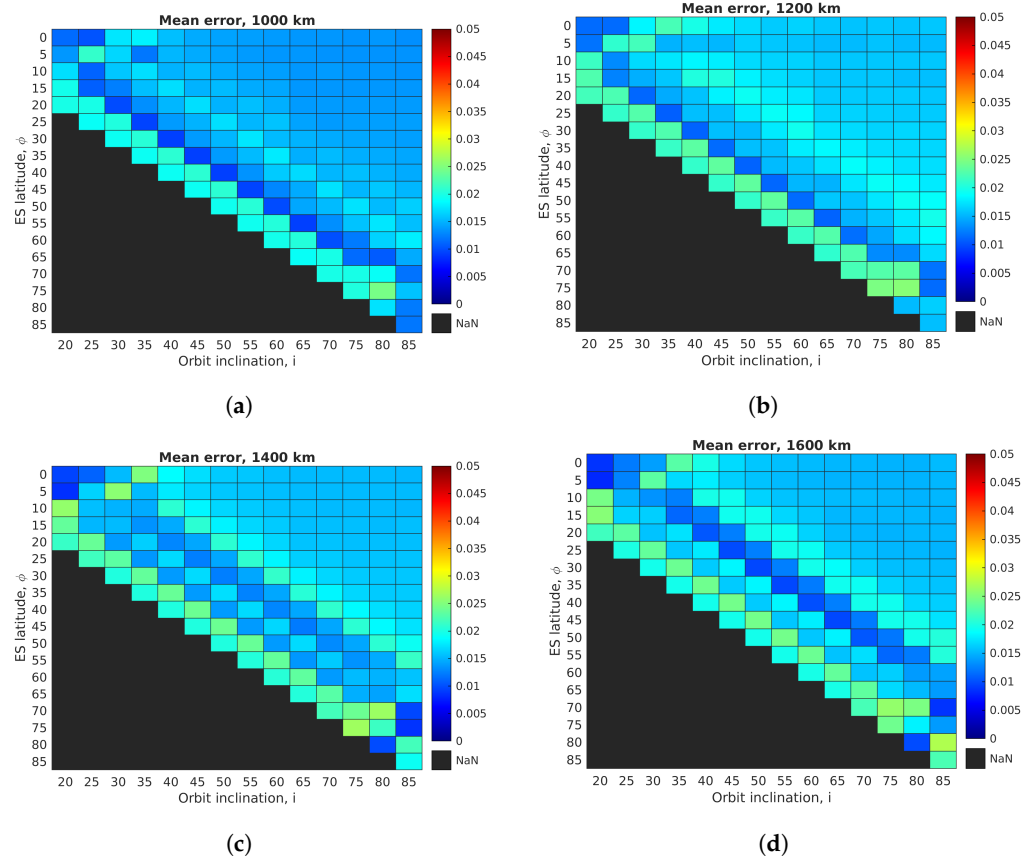


Figure A1. Cont.

Appendix C

This appendix contains the well-known four-point-mesh interpolation method, which was applied in this paper to determine the shape, a , and rate, b , parameters from matrices A_h and B_h for a given set of coordinates (i, ϕ) . More interpolation methods are widely available in the literature.

Interpolation for a Four-Point Mesh

The bilinear method is proposed as the method to find the query point inside the mesh since it is a well-known method and widely applied for interpolation.

We can obtain the values for a query point as in Figure A2 for a shape parameter value a using bilinear interpolation as follows

$$a(\phi, i) = w_1 a(\phi_2, i_1) + w_2 a(\phi_1, i_1) + w_3 a(\phi_2, i_2) + w_4 a(\phi_1, i_2), \quad (A1)$$

similarly, we can obtain the scale parameter, b , using bilinear interpolation as follows

$$b(\phi, i) = w_1 b(\phi_2, i_1) + w_2 b(\phi_1, i_1) + w_3 b(\phi_2, i_2) + w_4 b(\phi_1, i_2), \quad (A2)$$

where the wights w_1, w_2, w_3 and w_4 are given by

$$w_1 = (i_2 - i)(\phi_1 - \phi) / [(i_2 - i_1)(\phi_1 - \phi_2)] \quad (A3)$$

$$w_2 = (i_2 - i)(\phi - \phi_2) / [(i_2 - i_1)(\phi_1 - \phi_2)] \quad (A4)$$

$$w_3 = (i - i_1)(\phi_1 - \phi) / [(i_2 - i_1)(\phi_1 - \phi_2)] \quad (A5)$$

$$w_4 = (i - i_1)(\phi - \phi_2) / [(i_2 - i_1)(\phi_1 - \phi_2)] \quad (A6)$$

where the known values for $a(i_n, \phi_m), \dots, a(i_{n+1}, \phi_{m+1})$ and $b(i_n, \phi_m), \dots, b(i_{n+1}, \phi_{m+1})$, can be obtained from matrices A_h and B_h .

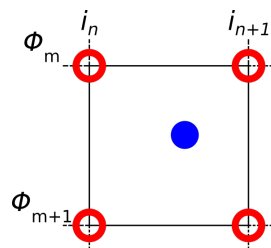


Figure A2. $F_\theta(\Theta)$ for two orbit configurations.

References

1. Crowe, K.; Raines, R. A model to describe the distribution of transmission path elevation angles to the Iridium and Globalstar satellite systems. *IEEE Commun. Lett.* **1999**, *3*, 242–244. [CrossRef]
2. Li, S.Y.; Liu, C. An analytical model to predict the probability density function of elevation angles for LEO satellite systems. *IEEE Commun. Lett.* **2002**, *6*, 138–140. [CrossRef]
3. Corazza, G.; Vatalaro, F. A statistical model for land mobile satellite channels and its application to nongeostationary orbit systems. *IEEE Trans. Veh. Technol.* **1994**, *43*, 738–742. [CrossRef]
4. Davoli, F.; Kourogorgas, C.; Marchese, M.; Panagopoulos, A.; Patrone, F. Small satellites and CubeSats: Survey of structures, architectures, and protocols. *Int. J. Satell. Commun. Netw.* **2019**, *37*, 343–359. [CrossRef]
5. del Portillo, I.; Cameron, B.G.; Crawley, E.F. A technical comparison of three low earth orbit satellite constellation systems to provide global broadband. *Acta Astronaut.* **2019**, *159*, 123–135. [CrossRef]

6. Popescu, O. Power Budgets for CubeSat Radios to Support Ground Communications and Inter-Satellite Links. *IEEE Access* **2017**, *5*, 12618–12625. [[CrossRef](#)]
7. Hu, J.; Li, G.; Bian, D.; Gou, L.; Wang, C. Optimal Power Control for Cognitive LEO Constellation With Terrestrial Networks. *IEEE Commun. Lett.* **2020**, *24*, 622–625. [[CrossRef](#)]
8. Chobotov, V.A. *Orbital Mechanics*, 3rd ed.; AIAA: Reston, VA, USA 2002.
9. Gongora-Torres, J.M.; Vargas-Rosales, C.; Aragón-Zavala, A.; Villalpando-Hernandez, R. Link Budget Analysis for LEO Satellites Based on the Statistics of the Elevation Angle. *IEEE Access* **2022**, *10*, 14518–14528. [[CrossRef](#)]
10. Kolawole, M.O. *Satellite Communication Engineering*; Marcel Dekker, Inc.: New York, NY, USA, 2002; Chapter 2.
11. Zhengsheng, C.; Qinghua, Z.; Xuerui, L.; Dashuang, S.; Hao, L.; Runtao, Z.; Jinlong, C. A reference satellite selection method based on maximal elevation angle during the observation period. In Proceedings of the 2017 Forum on Cooperative Positioning and Service, CPGPS 2017, 2017, number 2017 Forum on Cooperative Positioning and Service, CPGPS 2017, Harbin, China, 19–21 May 2017; pp. 268–272.
12. Seyedi, Y. A Trace-Time Framework for Prediction of Elevation Angle Over Land Mobile LEO Satellites Networks. *Wirel. Pers. Commun.* **2012**, *62*, 793–804. [[CrossRef](#)]
13. Su, Y.; Liu, Y.; Zhou, Y.; Yuan, J.; Cao, H.; Shi, J. Broadband LEO Satellite Communications: Architectures and Key Technologies. *IEEE Wirel. Commun.* **2019**, *26*, 55–61. [[CrossRef](#)]
14. Qu, Z.; Zhang, G.; Cao, H.; Xie, J. LEO Satellite Constellation for Internet of Things. *IEEE Access* **2017**, *5*, 18391–18401. [[CrossRef](#)]
15. Lopez-Salamanca, J.J.; Seman, L.O.; Berejuck, M.D.; Bezerra, E.A. Finite-State Markov Chains Channel Model for CubeSats Communication Uplink. *IEEE Trans. Aerosp. Electron. Syst.* **2020**, *56*, 142–154. [[CrossRef](#)]
16. Tropea, M.; De Rango, F. A Comprehensive Review of Channel Modeling for Land Mobile Satellite Communications. *Electronics* **2022**, *11*, 820. [[CrossRef](#)]
17. Saeed, N.; Elzanaty, A.; Almorad, H.; Dahrouj, H.; Al-Naffouri, T.Y.; Alouini, M.S. CubeSat Communications: Recent Advances and Future Challenges. *IEEE Commun. Surv. Tutor.* **2020**, *22*, 1839–1862. [[CrossRef](#)]
18. Kodheli, O.; Lagunas, E.; Maturo, N.; Sharma, S.K.; Shankar, B.; Montoya, J.F.M.; Duncan, J.C.M.; Spano, D.; Chatzinotas, S.; Kisseleff, S.; et al. Satellite Communications in the New Space Era: A Survey and Future Challenges. *IEEE Commun. Surv. Tutor.* **2021**, *23*, 70–109. [[CrossRef](#)]
19. Arapoglou, P.D.; Liolis, K.; Bertinelli, M.; Panagopoulos, A.; Cottis, P.; De Gaudenzi, R. MIMO over Satellite: A Review. *IEEE Commun. Surv. Tutor.* **2011**, *13*, 27–51. [[CrossRef](#)]
20. Baeza, V.M.; Lagunas, E.; Al-Hraishawi, H.; Chatzinotas, S. An Overview of Channel Models for NGSO Satellites. In Proceedings of the 2022 IEEE 96th Vehicular Technology Conference (VTC2022-Fall), London, UK, 26–29 September 2022; pp. 1–6. [[CrossRef](#)]
21. Loo, C. A statistical model for a land mobile satellite link. *IEEE Trans. Veh. Technol.* **1985**, *34*, 122–127. [[CrossRef](#)]
22. Lutz, E.; Cygan, D.; Dippold, M.; Dolainsky, F.; Papke, W. The Land Mobile Satellite Communication Channel-Recording, Statistics, and Channel Model. *IEEE Trans. Veh. Technol.* **1991**, *40*, 375–386 [[CrossRef](#)]
23. Abdi, A.; Lau, W.C.; Alouini, M.S.; Kaveh, M. A new simple model for land mobile satellite channels: First- and second-order statistics. *IEEE Trans. Wirel. Commun.* **2003**, *2*, 519–528. [[CrossRef](#)]
24. Fontan, F.; Vazquez-Castro, M.; Cabado, C.; Garcia, J.; Kubista, E. Statistical modeling of the LMS channel. *IEEE Trans. Veh. Technol.* **2001**, *50*, 1549–1567. [[CrossRef](#)]
25. National Aeronautics and Space Administration. General Mission Analysis Tool (GMAT) Version R2022a. Available online: <http://sourceforge.net/projects/gmat/> (accessed on 15 March 2022).
26. Gongora-Torres, J.M. Time Series for LEO Available online:.. (accessed on 17 March 2022). [[CrossRef](#)]
27. Al-Hraishawi, H.; Chougrani, H.; Kisseleff, S.; Lagunas, E.; Chatzinotas, S. A Survey on Nongeostationary Satellite Systems: The Communication Perspective. *IEEE Commun. Surv. Tutor.* **2022**, *25*, 101–132. [[CrossRef](#)]
28. Papoulis, A. *Probability, Random Variables, and Stochastic Processes*; McGraw-Hill: New York, NY, USA, 1984. [[CrossRef](#)]

Disclaimer/Publisher’s Note: The statements, opinions and data contained in all publications are solely those of the individual author(s) and contributor(s) and not of MDPI and/or the editor(s). MDPI and/or the editor(s) disclaim responsibility for any injury to people or property resulting from any ideas, methods, instructions or products referred to in the content.